Analyst

PAPER

View Article Online
View Journal | View Issue

Check for updates

Cite this: *Analyst*, 2025, **150**, 3946

Deciphering radiopharmaceutical mechanisms through integrated proteomic and PTM-proteomic profiling†

Xuefang Dong, ‡[a,b] Xinlian Ding,‡[a,b] Lingyan Yuan,[c] Yun Cui,[a,b] Zhitong Bing,[c] Long Yu,[a,b] Lei Yang,*[c] Xiuling Li *[a,b] and Xinmiao Liang [a,b]

Drug-regulated protein post-translational modifications (PTMs) enable the identification of modulated pathways and the revelation of phenotypic responses in diseases. However, the integrated regulatory mechanisms of radiopharmaceuticals across the proteomic and PTM landscapes remain poorly characterized. To address this gap, this study presents a quantitative multi-level proteomic analysis to assess regulated PTMs and pathway engagement. Quantitative glycoproteomics, phosphoproteomics, and global proteomics were performed using tumor tissues from radiopharmaceutical-treated mouse models. By analyzing subcellular signaling pathways with site-specific PTMs, differentially expressed molecular signatures were identified with radiopharmaceutical action. Our study provides a comprehensive landscape of the global proteome and PTM-proteome for radiopharmaceutical regulation. These findings uncover multi-level cellular molecular mechanisms involving DNA repair, extracellular matrix organization, and metabolic regulation. These findings elucidate the molecular mechanism of radiopharmaceuticals at the proteomic and PTM-proteomic levels, offering valuable insights for radiopharmaceutical development.

Received 1st July 2025,
Accepted 8th July 2025

DOI: 10.1039/d5an00690b

rsc.li/analyst

Open Access Article. Published on 30 July 2025. Downloaded on 6/14/2026 5:43:12 PM.
This article is licensed under a Creative Commons Attribution-NonCommercial 3.0 Unported Licence.

1. Introduction

Radiopharmaceuticals exert their therapeutic effects through emitting α-particles or β-particles following the decay of unstable nuclei.[1] Generally, radiopharmaceuticals are employed in cancer diagnosis and prognosis monitoring, as they can be visualized by nuclear medicine imaging techniques due to the agent's targeting effectiveness.[2] In recent years, with the increasing availability of diverse radiopharmaceuticals for treating various diseases, particularly cancers, radiopharmaceuticals have also shifted from purely visualized diagnosis to precise targeted therapy.[3] The primary mechanism of action (MoA) of radiopharmaceuticals involves inducing DNA damage within tumor cells.[4] Energy from radiopharmaceuticals traverses tissues, deposits inside cells, and causes single-strand breaks (SSB) or double-strand breaks (DSB) in DNA.[5] Although DNA damage is widely recognized as the fundamental MoA of radiopharmaceuticals, the intricate molecular mechanisms underlying this process remain insufficiently studied. The most widely used approaches for investigating the mechanisms of radiopharmaceuticals include comet assay (single-cell gel electrophoresis), ELISA (enzyme-linked immunosorbent assay), immunoblotting (western blotting), immunohistochemistry (IHC), flow cytometry, and fluorescence microscopy.[6–9] However, these approaches are often target-specific and do not allow for a comprehensive evaluation of the overall molecular effects of radiopharmaceuticals.

Proteins serve as key executors of biological functions and are also targets for many pharmaceuticals.[10,11] Protein post-translational modifications (PTMs) impact numerous biological processes and pathogenesis, and studies on PTMs can elucidate drug mechanisms from diverse molecular perspectives.[12,13] With the advancement of mass spectrometry technology, proteomics can simultaneously identify and quantify thousands of proteins and their PTMs, providing valuable insights into the interpretation of drug MoA.[10] Recent advancements in proteomic, phosphoproteomic and glycoproteomic research enable large-scale identification of target proteins of cancer drugs and the investigation of resistance mechanisms across diverse drugs.[13–16] Although proteome and PTM studies offer significant advantages in exploring drug

[a]*Ganjiang Chinese Medicine Innovation Center, Nanchang, 330000, P. R. China*
[b]*State Key Laboratory of Phytochemistry and Natural Medicines. Dalian Institute of Chemical Physics, Chinese Academy of Sciences, Dalian, 116023, P. R. China. E-mail: lixiuling@dicp.ac.cn*
[c]*Department of Computational Physics, Institute of Modern Physics, Chinese Academy of Sciences, Lanzhou, China School of Nuclear Science and Technology, University of Chinese Academy of Sciences, Beijing, China. E-mail: lyang@impcas.ac.cn*

†Electronic supplementary information (ESI) available. See DOI: https://doi.org/10.1039/d5an00690b

‡Theses authors contribute equally.

This journal is © The Royal Society of Chemistry 2025

Open Access Article. Published on 30 July 2025. Downloaded on 6/14/2026 5:43:12 PM. This article is licensed under a Creative Commons Attribution-NonCommercial 3.0 Unported Licence.

mechanisms, the MoA of the radiopharmaceuticals has not been thoroughly investigated using proteomics and PTM profiling. To address this gap, we performed an integrated proteomic analysis to investigate the MoA of a radiopharmaceutical.

In a previous work, we constructed an integrated platform that can perform multi-level proteomic research, including glycoproteomics, phosphoproteomics and proteomics.[17] The integration of diverse omics data enables a comprehensive molecular-level analysis of drug mechanisms, effectively complementing traditional approaches to studying the MoA of drugs. In this study, we utilized our multi-level proteomic platform to investigate the biological responses of the radiopharmaceutical ^{225}Ac in a colon cancer mouse model, achieving a comprehensive study of the MoA of radiopharmaceuticals across global proteomic, glycoproteomic, and phosphoproteomic landscapes. We found that ^{225}Ac strongly affected the mitochondrial energy metabolism of tumor cells, subsequently leading to the significant activation of immune and hemostatic functions. Additionally, we discovered that the abundance of high-mannose glycan structures significantly decreased following radiopharmaceutical treatment. Moreover, we highlighted the phosphorylation changes of proteins involved in DNA damage and repair pathways. Collectively, our results described the mechanism of radiopharmaceuticals from a unique molecular perspective and provided a more thorough molecular profiling for MoA.

2. Materials and methods

2.1. Animal studies

All experimental procedures were carried out according to the Guidelines for the Care and Use of Laboratory Animals, and approval was obtained from the Animal Ethics Committee of the Ganjiang traditional Chinese medicine innovation center (permit number: GJCMIC2024-013). Eight 5-week-old male Balb/c mice were used to construct a CT26 tumor-bearing model and randomly assigned to a radiopharmaceutical treatment group (n = 4) and a control group (n = 4). CT26 mouse colon cancer tissue was digested with trypsin to form a cell suspension, and the cell concentration was adjusted to 1×10^7 cells per mL. The right side of the back of mice was used for subcutaneous inoculation with 100 μL cell suspension (about 1×10^6 cells) under aseptic procedure to ensure that there was no fluid leakage during the injection and obvious subcutaneous nodules were formed. Seven days after inoculation, the mice were observed daily to ensure animal welfare, and therapeutic efficacy was assessed by caliper (volume (mm^3) = 0.52 × length × width^2) every two days.[18,19]

CT26 tumor-bearing mice were randomly assigned to treatment groups when the mean tumor volume reached 100 mm^3. The experimental group received an intravenous injection of 0.4 μCi of ^{225}Ac, solubilized in a solution of 2 M ammonium acetate and 150 mg mL^{-1} L-ascorbic acid. The control group was administered the solvent vehicle alone. The tumor diameter, body weight, and overall animal well-being were monitored every two days. The study was conducted for two weeks, after which the mice were euthanized. Mice with ulcerated tumors, which were observed across all groups, were euthanized prior to the study endpoint and excluded from the analysis.

2.2. Reagents and materials

Trypsin was purchased from Sigma-Aldrich (USA). Chemical reagents including iodoacetamide (IAA), 1,4-dithiothreitol (DTT), acetonitrile (ACN, HPLC grade), ammonium bicarbonate, urea, ammonium hydroxide, formic acid and trifluoroacetic acid (TFA) were obtained from Sigma-Aldrich. Deionized water was prepared using a Milli-Q system (18.2 M Ω cm, Bedford, MA, USA). In this work, we utilized the click-maltose material for N-linked glycopeptide enrichment. The click-maltose material, developed by our group previously,[20,21] has demonstrated exceptional selectivity and robustness in capturing N-linked glycopeptides. The click-maltose material was synthesized by linking alkynyl-derivatized maltose to azide-derivatized silica *via* click chemistry. The resulting flexible saccharide chain structure remarkably enhances the hydrogen-bonding interactions between the glycans of the glycopeptides and the matrix, enabling efficient enrichment of glycopeptides while minimizing non-specific binding. Its performance has been validated by multiple independent research groups,[22,23] underscoring its reliability and reproducibility. The phosphopeptide enrichment was performed using a commercialized Ti^{4+}-IMAC material (J&K Scientific Ltd Cat. No. 2749380), whose enrichment efficiency has been validated in previous studies.[17,24,25]

2.3. Sample preparation

Tumors resected 48 hours after treatment were isolated using scissors and tweezers and then homogenized in an ice bath *via* sonication (20 W, 3 s ultrasound with a 7 s interval for 3 min) in a urea buffer containing a phosphatase inhibitor cocktail (1 μL per 100 μL of buffer). The suspension was centrifuged at 14 000 rpm for 20 min, and the supernatant was quantified by the BCA protein assay. Then, 1 mg of proteins was dissolved in 200 μL urea buffer and incubated with 10 μL of 200 mM DTT at 56 °C for 45 min. After the addition of 10 μL of 800 mM IAA, the reaction mixture was allowed to react in the dark at room temperature for 30 min. The mixture was diluted to 2 mL with 50 mM NH_4HCO_3 and incubated with trypsin (1 : 50, w/w) at 37 °C for 16 h. The obtained tumor lysate digest was lyophilized and stored at −80 °C for subsequent analyses.

2.4. Simultaneous enrichment of N-linked glycopeptides and phosphopeptides

The specific glycopeptide enrichment procedures are as follows. First, 3 mg of click-maltose material was suspended in 60 μL ACN and packed into the bottom of a 10 μL pipette tip. The tip was conditioned and equilibrated with 100 μL 80% ACN/1% TFA. Then, 100 μg peptide sample was desalted with C18, dissolved in 100 μL 80% ACN/1% TFA and loaded onto the tip. The tip was rinsed four times with 50 μL 80% ACN/1% TFA. The flow-through from the click-maltose tip was collected for subsequent phosphopeptide enrichment. The glycopep-

Open Access Article. Published on 30 July 2025. Downloaded on 6/14/2026 5:43:12 PM. This article is licensed under a Creative Commons Attribution-NonCommercial 3.0 Unported Licence.

tides were subsequently eluted with 60 μL of 30% ACN/1% FA, dried, and stored at −80 °C prior to LC-MS/MS analysis.

The dried flow-through from glycopeptide enrichment was resuspended in 80% ACN/2% TFA. Then, 5 mg of Ti^{4+}-IMAC material was packed into the 10 μL pipette tip and equilibrated with 50 μL 80% ACN/2% TFA. Each sample then was loaded onto the Ti^{4+}-IMAC tip. After the Ti^{4+}-IMAC tip was washed three times with 50 μL 80% ACN/2% TFA and 80% ACN, respectively, bound phosphopeptides were eluted with 10% ammonium hydroxide and dried before LC-MS/MS analysis.

2.5. LC-MS/MS analysis

During multi-sample experiments, the enriched N-linked glycopeptides and phosphopeptides were separated and identified using an EASY-nLC 1200 liquid chromatography system (Thermo Scientific, United States) coupled to an Orbitrap Exploris™ 480 mass spectrometer (Thermo Scientific, United States). A homemade C18 analytical column (150 μm × 150 mm, 2 μm) was used to separate peptides. Mobile phase A was 0.1% FA and mobile phase B was 80% ACN/0.1% FA. The flow rate was set at 400 nL min^{-1}. The phosphopeptide gradient elution is as follows: 1%–5% B, 3 min; 5%–32% B, 50 min; 32%–90% B, 2 min; 90% B, 5 min. The N-linked glycopeptide gradient elution is as follows: 3%–10% B, 6 min; 10%–40% B, 100 min; 40%–90% B, 4 min; 90%B, 10 min. The data of N-linked glycopeptides were acquired in the data-dependent acquisition (DDA) mode using an Orbitrap Exploris™ 480 mass spectrometer with the following settings: ion transport capillary temperature: 320 °C; spray voltage: 2.5 kV; full MS resolution: 60 000; normalized AGC target for full MS: 300%; scan range for full MS: 350–1500 *m*/*z*; maximum injection time for full MS: 40 ms; RF lens: 40%; MS2 resolution: 30 000; normalized AGC target for MS2: 75%; maximum inject time for MS2: 80 ms; top speed mode cycle time for data-dependent MS/MS: 2 s; number of microscans for data-dependent MS/MS: 1 scan per s (charge state 2–6); dynamic exclusion duration: 45 s; precursor intensity threshold: $8E^3$; and mass tolerance: ±10 ppm. Normalized collision energy was set at 20%, 30% and 40%. For the further analysis of phosphopeptides, full MS resolutions for the data-independent acquisition (DIA) experiments were set to 600 000 at *m*/*z* 200 and full MS AGC target was 300% with an IT of 40 ms. The mass range was set to 350–1500 *m*/*z*. The AGC target value for fragment spectra was set at 2000%. Fifty-nine windows of 6.7 Da were used with an overlap of 1 Da. Normalized collision energy was set at 32%. All data were acquired in the profile mode using positive polarity, peptide match was set to "off", and isotope exclusion was set to "on".

2.6. Data processing

In this study, glycopeptides were analyzed directly by mass spectrometry without prior enzymatic release of the glycans, which is a general and mature method in glycoproteomics.[26–31] The objective of intact glycopeptide analysis was to retain site-specific glycan information, which enables the acquisition of detailed information about each individual glycan structure present at each specific glycosylation site. For *N*-glycosylation identification and quantification, raw files were analyzed using PMI Byos (version 5.4.52, Protein Metrics, Inc.). All the MS raw data files were searched against the database downloaded from UniProt-Mouse database (17 747 entries) and a Byos built-in glycan database of 309 *N*-glycans for glycopeptide compositional analysis using the Byos software. Searches were conducted with the fragmentation type set to as higher-energy collisional dissociation (HCD). The database searching parameters of precursor and fragment ion tolerance were set at 10 and 20 ppm, respectively. Enzyme specificity was set to trypsin allowing for up to two missed cleavages. Carbamidomethylation of cysteine residues (C; +57.022 Da) was set as the fixed modification. Oxidation on the methionine residue (M; +15.995 Da) was set as the variable modification. The false discovery rate (FDR) for glycopeptide spectrum match (GPSM) and protein-level was less than 1%. The scores of N-linked glycopeptides were no less than 150. The identification and quantification of phosphopeptide were conducted using Spectronaut 19 (Biognosys AG, Switzerland) against the UniProt-Mouse database (17 747 entries) with default settings for direct DIA analysis. The FDR cutoff on the precursor level was 1% and protein level was 1%. The normalization strategy was set as local normalization. Carbamidomethylation of cystine was set as fixed modification. The oxidation of methionine, phosphorylation (localization probability >0.75), and protein N-terminal acetylation were set as variable modifications.

Quantifiable phosphopeptides and glycopeptides were filtered with more than half valid quantitative values in each group. The intensities were subsequently log2-transformed, and missing values were imputed using the Perseus software. Significant changes in phosphopeptides and glycopeptides were identified using a two-sample *t*-test, with a *p*-value threshold of 0.05 and a minimum fold change (FC) of 1.5. Statistical analysis of data was performed using the GraphPad Prism 9 and Perseus 2.0.11 software. The proteomics data were processed using identical filtering criteria as applied to the phosphoproteomics and glycoproteomics data.

To integrate the glycoproteomic, phosphoproteomic, and proteomic datasets, we employed a strategy whereby multi-omics data were linked *via* shared UniProt IDs. For each protein, we compared changes in its different modifications derived from glycoproteomic and phosphoproteomic analyses against variations in its total abundance from proteomic analysis. Using the pathway analysis tool Metascape, we annotated differentially expressed PTMs or proteins into functional pathways and conducted joint enrichment analyses by integrating information from distinct modifications.

3. Results

3.1. Integrated multi-level proteomic workflow for assessing radiopharmaceutical mechanisms

To investigate the molecular alterations induced by ^{225}Ac, we employed a previously developed proteomic platform to study the MoA of ^{225}Ac on a multi-level proteomic scale. Leveraging our established integrated multi-level proteomic sample prepa-

 This journal is © The Royal Society of Chemistry 2025

Open Access Article. Published on 30 July 2025. Downloaded on 6/14/2026 5:43:12 PM.
This article is licensed under a Creative Commons Attribution-NonCommercial 3.0 Unported Licence.

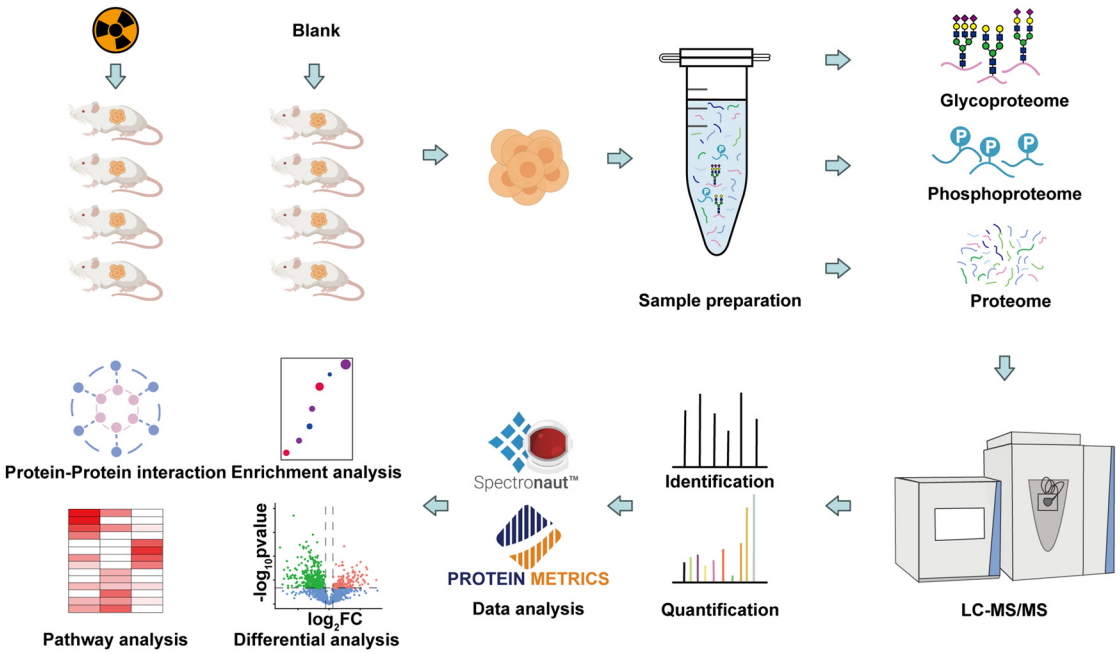

Fig. 1 Schematic overview of the experimental workflow. The multi-level proteomic workflow for glycoproteome, phosphoproteome, and proteome analyses for the MoA of radiopharmaceuticals.

ration platform, we performed a comprehensive profiling of the glycoproteome, phosphoproteome and proteome in tumor samples from mouse models. The obtained tumor samples were processed *via* protein extraction, digestion, glycopeptides and phosphopeptides enrichment. The prepared samples were then analyzed by LC-MS/MS, and the MS data were interpreted using the PMI Byos and Spectronaut software. We conducted a multifaceted analysis to elucidate differently expressed glycoproteome, phosphoproteome and proteome for biological functions, protein–protein interactions, and pathway enrichment (Fig. 1).

3.2. Glycoproteomic analysis of radiopharmaceutical-induced differential glycosylation

Glycosylation is one of the most prevalent and essential PTMs, and plays a pivotal role in many biological processes, especially in protein folding, cell adhesion, cellular signaling, pathogenesis of different diseases and MoA of various drugs.[32,33] However, the MoA of radiopharmaceutical at the glycoproteomic level has not yet been reported. In this work, we profiled the glycoproteome of tumor samples after radiopharmaceutical treatment by identifying and quantifying glycan structures, glycosylation sites, and glycosylation-related enzymes. In total, we identified 18 613 site-specific glycans mapping to unique 3519 *N*-glycosylation on 1250 glycoproteins. First, we analyzed the alterations of different glycan types and found that the abundance of sialylated, fucosylated and truncated glycan structures showed an increasing trend, whereas the abundance of high-mannose glycan structures decreased significantly following radiopharmaceutical treatment (Fig. 2A). Glycosylation changes implied alterations in glycosylation-related glycosidases and glycosyltransferases, and we therefore investigated relative abundance changes of these enzymes at the proteomic level. A total of nine glycosidases and glycosyltransferases changed their relative abundance in the proteome dataset (Fig. 2B), indicating the effect of the radiopharmaceuticals on glycosylation. Among these, the abundance of Ganab was significantly decreased in the radiopharmaceutical-treated group.

We quantified the relative abundance of the top 10 glycans and found that the relative abundance of high-mannose glycans (H5N2, H6N2, H7N2, H8N2 and H9N2) decreased after radiopharmaceutical treatment, with the exception of H5N2 (Fig. 2C). Our results also revealed that the abundance of both sialofucosylated and fucosylated glycans (H6N4F1G1 and H5N4F1G2) decreased, whereas the abundance of fucosylated-only or sialylated-only glycans (H5N4G2, H3N4F1 and H6N5G3) increased in the radiopharmaceutical-treated group. In addition, we performed differential analysis of the glycan expression and identified 15 glycans that were significantly altered, including 11 glycans with decreased relative abundance and 4 glycans with increased relative abundance (Fig. 2D). Notably, 4 of 5 decreased sialylated glycans contained NeuGc modification. In contrast, the increased sialylated glycans contained NeuAc modification.

We further performed the analysis of differentially expressed site-specific glycans (Fig. 3A) and identified 536 significantly altered site-specific glycans, including 156 with increased and 380 with decreased relative abundance. Among these, C1qa–N734–H8N2 exhibited the most significant downregulation following radiopharmaceutical treatment. The detailed information on *N*-glycosylation identifications of

Open Access Article. Published on 30 July 2025. Downloaded on 6/14/2026 5:43:12 PM.
This article is licensed under a Creative Commons Attribution-NonCommercial 3.0 Unported Licence.

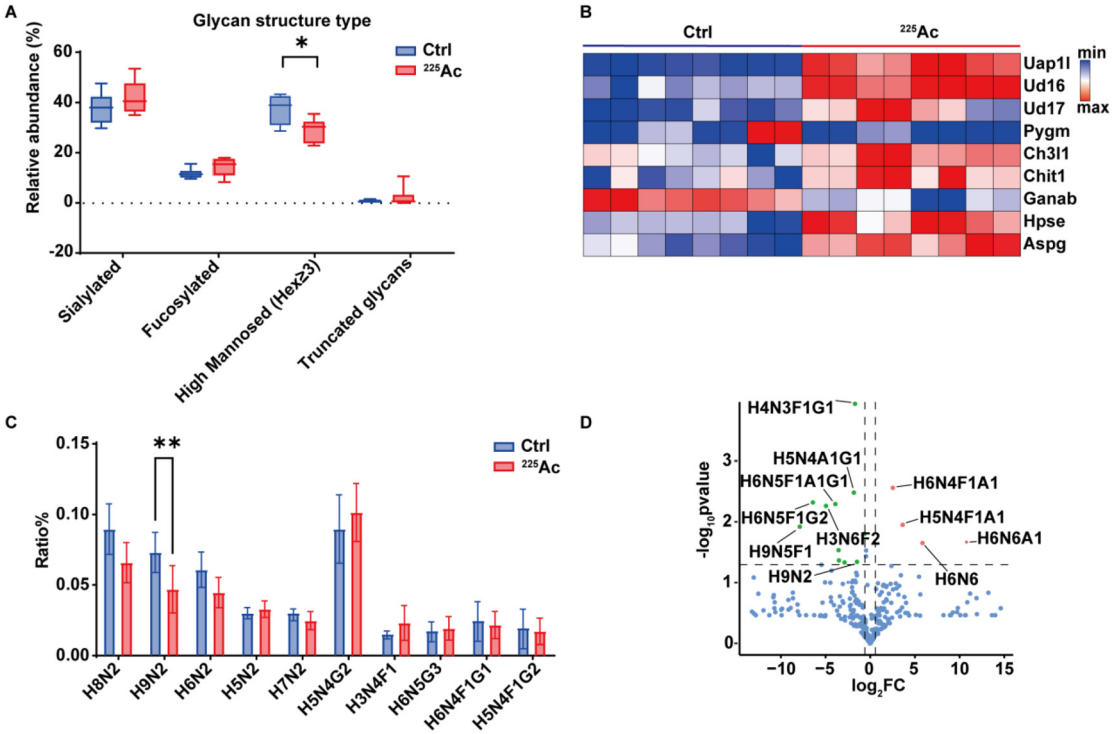

Fig. 2 Glycosylation profiling of tumors treated with radiopharmaceuticals based on glycoproteomic data. (A) Comparison of the relative abundance of glycan types between control and radiopharmaceutical-treated groups. (B) Heatmap showing the relative abundance of identified glycosidases and glycosyltransferases at the proteomic level. (C) Comparison of the relative abundance of the top 10 glycans. (D) Volcano plot of differentially expressed glycans. Glycan compositions are annotated using the following symbols: H = Hexose, N = *N*-acetylhexosamine, A = *N*-acetylneuraminic acid (NeuAc), G = *N*-glycolylneuraminic acid (NeuGc), and F = Fucose.

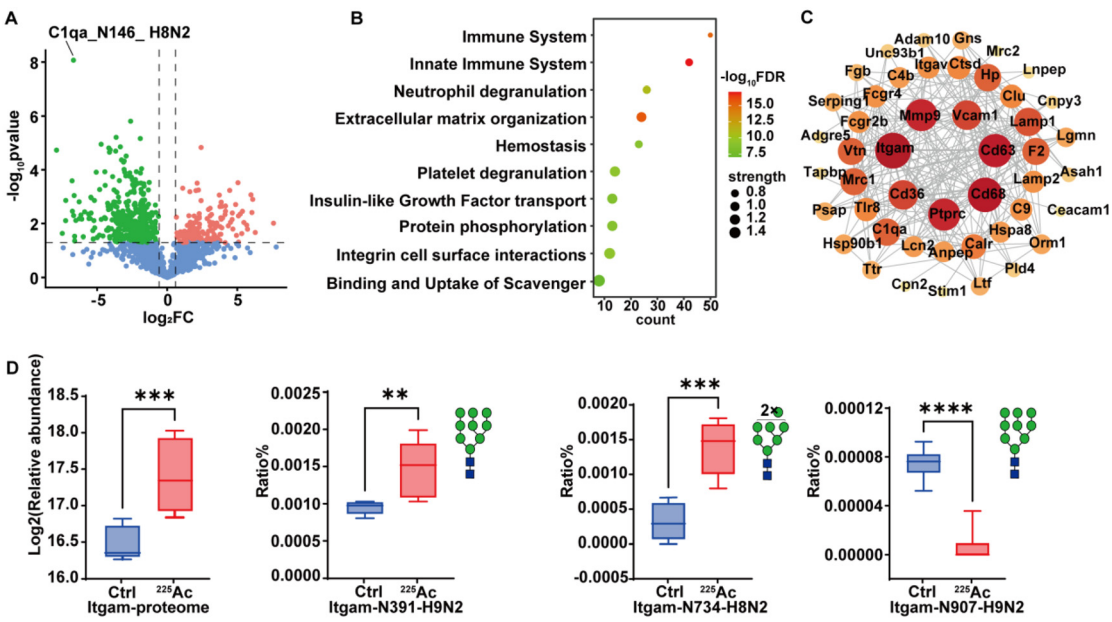

Fig. 3 Analysis of altered site-specific glycosylation in tumors treated with radiopharmaceuticals based on glycoproteomic data. (A) Volcano plot of differentially expressed site-specific glycopeptides. (B) Enriched pathways of glycoproteins with differentially expressed glycopeptides. (C) STRING PPI network of glycoproteins involved in the immune system. Node size indicates the degree of connectivity. (D) Altered relative abundance of Itgam at the proteomic level and its site-specific glycans at the glycoproteomic level. Shown are site-specific glycans on Itgam: H9N2 at N391, H8N2 at N734, and H9N2 at N907.

This journal is © The Royal Society of Chemistry 2025

Open Access Article. Published on 30 July 2025. Downloaded on 6/14/2026 5:43:12 PM.
This article is licensed under a Creative Commons Attribution-NonCommercial 3.0 Unported Licence.

C1qa glycosylation site N146 is provided in the ESI, Table S1.† We then performed gene ontology (GO) enrichment analysis on these glycoproteins with differentially expressed site-specific glycans to gain insights into their associated cellular functions and processes. The result indicated that these glycoproteins were significantly enriched in an immune system (Fig. 3B). In addition, the protein–protein interaction (PPI) network analysis of these glycoproteins revealed that the Itgam (integrin alpha M chain), a key mediator in the phagocytosis of complement-coated particles,[34] exhibited the highest degree of connectivity, suggesting its potential role in the anti-tumor effects of the radiopharmaceutical (Fig. 3C). We then investigated the glycosylation of Itgam and found that the relative abundance of 10 site-specific glycosylation of Itgam were upregulated, whereas 3 were significantly downregulated (Fig. 3D and S1†). In addition, we found the relative abundance of Itgam significantly upregulated in the proteome dataset (Fig. 3D). These results indicated that Itgam may be affected by the radiopharmaceutical treatment and may further contribute to anti-tumor effects. Although Itgam glycosylation has not been previously reported, the glycosylation changes in our study could provide novel insights into the MoA of the radiopharmaceuticals at the glycoproteomic level.

3.3. Phosphoproteomic profiling of radiopharmaceutical-induced kinase activity alterations

It is reported that DNA is the primary molecular target of radiopharmaceuticals and the SSBs or DSBs of DNA caused by radiopharmaceutical particles lead to cell death or mutations.[4] Phosphorylation plays a major regulatory role in DNA damage and repair.[35] Given the pivotal role of phosphorylation in DNA repair, we investigated the changes in the phosphorylation status of tumors following radiopharmaceutical treatment. A total of 12 490 phosphopeptides, corresponding to 11 721 phosphosites from 3352 phosphoproteins, were identified. Among these, 795 phosphosites were upregulated and 780 were downregulated (Fig. S2A†). Phosphoproteome comparison between the two groups revealed radiopharmaceutical-specific activated kinases *via* kinase substrate enrichment analysis (KSEA), including MAPK9 and CSNK2A1 (Fig. 4A). The suppressed kinases such as CDK1, CDK2 and CHEK1 were associated with DNA damage, cell cycle arrest and DNA repair. We then analyzed the pathways of phosphoproteins with differentially expressed phosphosites (Fig. 4B) and revealed that the relative pathways were significantly enriched in the cell cycle.

We also performed PPI analysis on phosphoproteins involved in the cell cycle pathway and identified the key roles of Tp53bp1 and Rb1 (Fig. S2B†). The tumor suppressor protein p53 is a central protein in DNA damage, and the extent of phosphorylation of p53 dictates cell survival or death.[36] We identified downregulated phosphorylation of Rb1cc1 and upregulated phosphorylation of Rb1 (Fig. S2C†), indicating that the Rb1 pathway was downregulated. This finding further supports that radiopharmaceuticals induced severe DNA damage, triggering DNA repair in tumor cells. Our phosphoproteomic analysis characterized radiopharmaceutical-induced site-specific phosphorylation alterations in key DNA damage and repair proteins, which are undetectable at other omic levels.

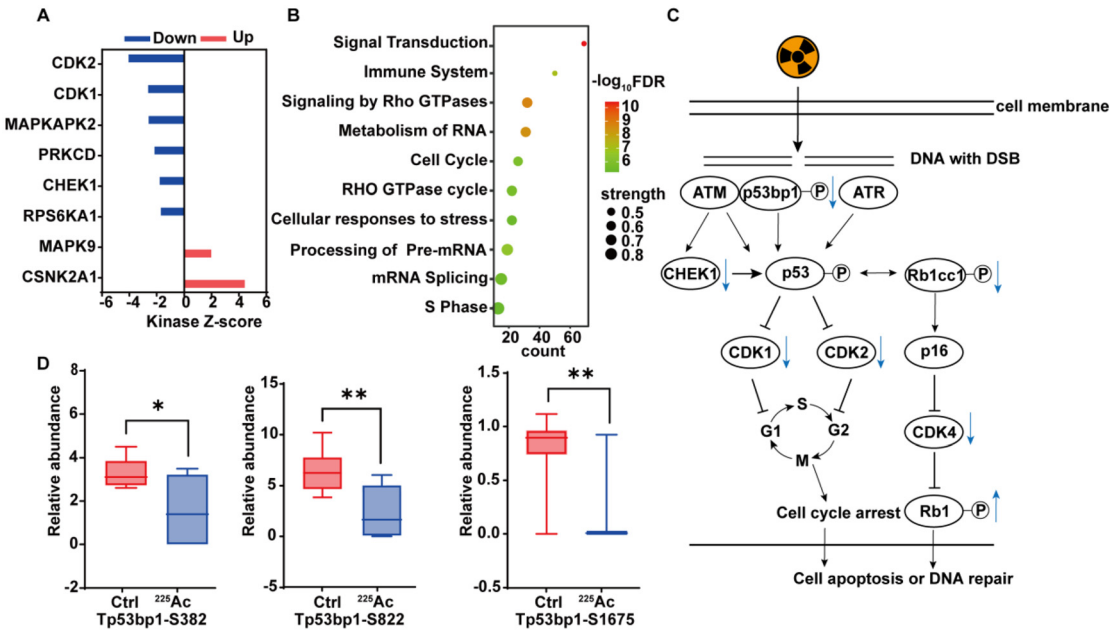

Fig. 4 Analysis of radiopharmaceutical-induced differentially expressed phosphosites and kinase activity alterations. (A) KSEA analysis of differentially expressed phosphosites. (B) Enriched pathways of phosphoproteins harboring differentially expressed phosphosites. (C) Hypothesized DNA damage and repair signaling alterations induced by radiopharmaceuticals. Phosphorylated proteins are labeled with ⓟ. (D) Decreased relative abundance of phosphorylation on S382, S822 and S1675 of Tp53bp1. Phosphorylation abundance was normalized by dividing the quantification intensity of each phosphosite by the quantification intensity of its corresponding protein, ensuring that reported changes reflect alterations in phosphorylation site occupancy relative to total protein abundance.

Open Access Article. Published on 30 July 2025. Downloaded on 6/14/2026 5:43:12 PM.
This article is licensed under a Creative Commons Attribution-NonCommercial 3.0 Unported Licence.

3.4. Proteomic insights into radiopharmaceutical-induced disruption of energy metabolism at the subcellular level

The glycoproteomic and phosphoproteomic analyses described above have demonstrated how radiopharmaceuticals induce alterations in PTMs. Subsequently, we extended our investigation to analyze the global proteomic changes induced by radiopharmaceuticals. A total of 5183 proteins were identified, of which 759 showed significant differential expression, including 497 upregulated and 262 downregulated ones (Fig. S3A†). Clustering analysis of the quantitative proteome further revealed distinct protein expression patterns, identifying one downregulated and two upregulated protein clusters. Collectively, these findings highlight the comprehensive impact of radiopharmaceuticals on protein expression and PTMs, providing insights into their potential mechanisms of action (Fig. 5A).

Proteins in cluster 1 were involved in the mitochondrial oxidative respiratory chain (Fig. 5B left), including mitochondrial complex I (ubiquinone oxidoreductase family, Ndu), mitochondrial complex III (cytochrome bc1 oxidoreductase, Uqcr) and mitochondrial complex IV (cytochrome C oxidase family, Cox). Tumor cells require sufficient energy to support their rapid division and proliferation, thus mitochondrial metabolism is essential for tumor cell immortalization.[37] Corroborating recent reports on targeted mitochondrial therapy in cancer,[38,39] our findings provide further evidence that the radiopharmaceuticals inhibit tumor development by strongly interfering with the mitochondrial respiratory chain. Proteins in cluster 2 were enriched in the hemostasis pathway (Fig. 5B middle). Cluster 3 was primarily enriched in the immune-related pathways (Fig. 5B, right), suggesting that radiopharmaceuticals might induce immune activation.

3.5. Multi-level proteomic integration: insights into radiopharmaceutical mechanisms through glycoproteome, phosphoproteome, and proteome synergy

Subcellular-level analysis further revealed potential mechanisms associated with distinct cellular compartments. Specifically, proteomic results indicated reduced activity of the tricarboxylic acid (TCA) cycle in the mitochondria and glycolysis in the cytoplasm. Furthermore, differentially expressed glycolytic enzymes involved in glycosylation processes localized to the endoplasmic reticulum and lysosome were identified (Fig. 6A). To further characterize the integrative effects of radiopharmaceuticals at the multi-level proteomic scale, we conducted a comprehensive analysis of the glycoproteome,

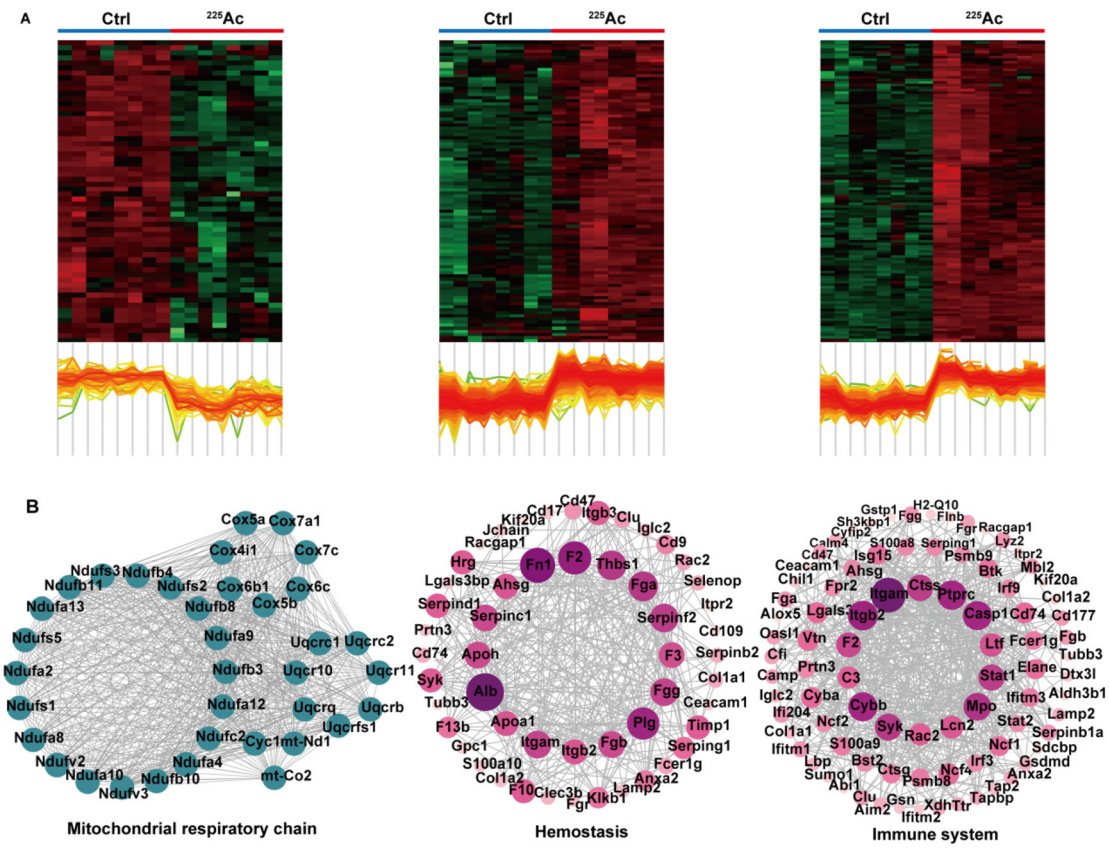

Fig. 5 Comprehensive analysis of the global proteome in tumors following radiopharmaceutical treatment. (A) Heatmap of relative protein abundance in cluster 1, cluster 2 and cluster 3. (B) PPI networks of proteins in corresponding clusters 1, 2 and 3. Gray lines represent protein–protein interactions. Node size and color intensity indicate the degree of connectivity with other proteins. Purple nodes denote upregulated proteins, while green nodes denote downregulated proteins.

This journal is © The Royal Society of Chemistry 2025

Open Access Article. Published on 30 July 2025. Downloaded on 6/14/2026 5:43:12 PM.
This article is licensed under a Creative Commons Attribution-NonCommercial 3.0 Unported Licence.

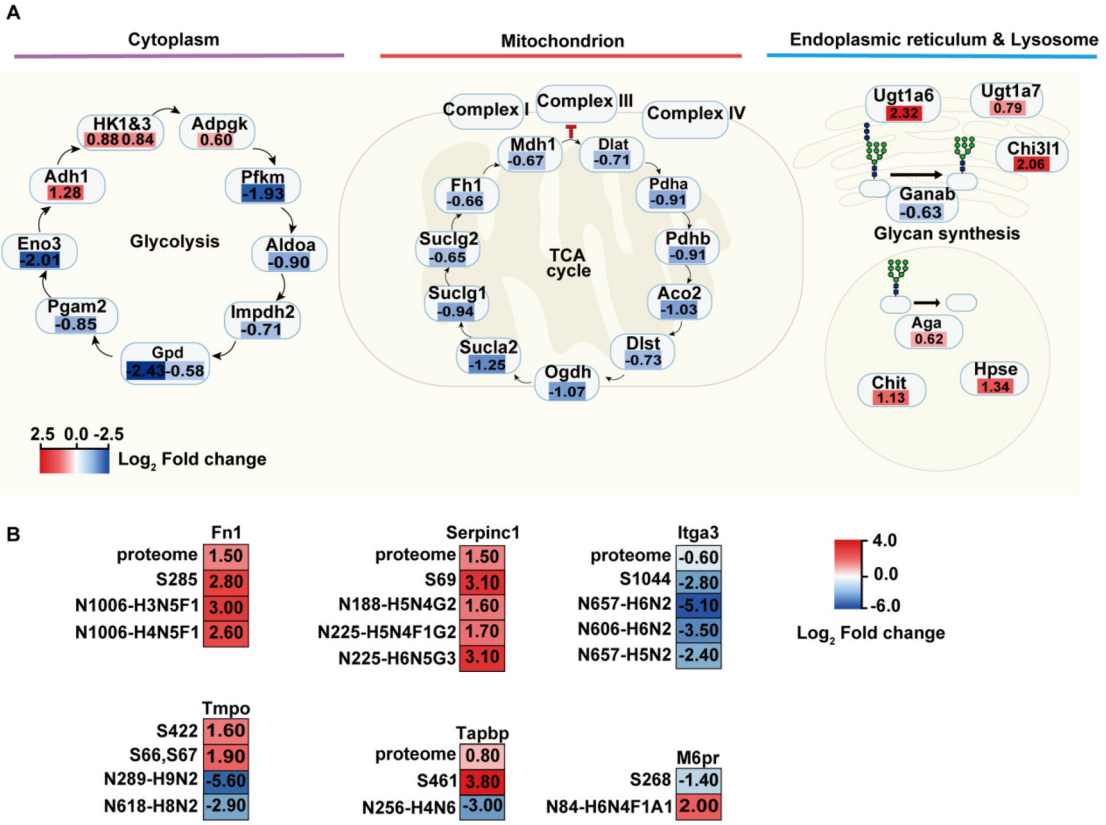

Fig. 6 Integrative proteomic and PTM analysis of radiopharmaceutical-treated tumor samples. (A) Hypothesized mechanism based on subcellular proteomic localization results. (B) Heatmap of log2 (fold change) for differentially expressed proteins across multi-omics datasets, highlighting key proteins and their associated PTMs sites. Red rectangles denote upregulated proteins, and blue rectangles denote downregulated proteins. The intensity of the color (red or blue) correlates directly with the absolute value of the log2 (fold change), where darker shades indicate greater expression changes.

phosphoproteome, and proteome. By comparing proteins with significant relative abundance changes across the three proteomic levels, we identified 78 proteins with concurrent changes in both the proteome and the phosphoproteome, 42 proteins with alterations in both the proteome and the glycoproteome, and 11 proteins with changes in both the glycoproteome and the phosphoproteome. These overlapping proteins may provide insights into the coordinated regulatory effects of radiopharmaceuticals on cellular processes (Fig. S3B†). Functional enrichment analysis using Metascape (Fig. S3C†) revealed that hemostasis was the most significantly enriched pathway across the proteome, phosphoproteome, and glycoproteome landscapes. Pathways exclusively enriched in the proteome included aerobic respiration, monocarboxylic acid metabolism, acyl–CoA metabolism, carbon metabolism, and mitochondrial protein degradation. Glycosylation was predominantly associated with pathways such as extracellular matrix organization, lysosomal processes, and protein processing in the endoplasmic reticulum. Phosphorylation was found to specifically influence chromatin conformation, mRNA metabolism, and DNA damage repair. Collectively, these findings validate the reliability of our results and are consistent with the aforementioned analysis.

We further conducted a site-specific analysis of proteins with significant alterations across the three omics layers (Fig. 6B). Notably, Fn1 and Serpinc1 with their corresponding PTM sites were found to be upregulated across the proteome, phosphoproteome, and glycoproteome landscape. As key components of the hemostasis pathway (Fig. 5B), the observed proteomic and PTM-proteomic differences may be closely associated with hemostatic function. Additionally, Itga3 and Tapbp were identified as related to the innate immune system. Itga3 showed decreased abundance across all three omics layers. In our study, Tapbp showed upregulated relative abundance in the proteome and phosphorylation at S461, while its relative abundance at the glycosylated site N256 with glycan H4N6 was downregulated. Tmpo and M6pr were not quantified at the proteome level but were quantified at glycoproteome and phosphoproteome levels. Tmpo showed upregulation at two phosphorylated sites (S422, S66 or S67) but downregulation at two glycosylated sites (N289 and N618), while M6pr showed downregulation at one phosphorylated site (S268) and upregulation at one glycosylated site (N84). These findings underscore that multi-level proteomic analysis can reveal distinct PTM alterations of the same protein in radiopharmaceutical-treated tumors, which would otherwise remain undetected in single-

Open Access Article. Published on 30 July 2025. Downloaded on 6/14/2026 5:43:12 PM.
This article is licensed under a Creative Commons Attribution-NonCommercial 3.0 Unported Licence.

omics analyses. Overall, this work enables a comprehensive investigation from multiple proteomic perspectives, offering novel molecular insights into the MoA of radiopharmaceuticals.

4. Discussion

In this study, we present a comprehensive proteomic study into the MoA of the radiopharmaceutical ^{225}Ac. We integrated multi-level proteomics to gain mechanistic insights into the radiopharmaceutical's impact across multiple dimensions, including phosphorylation and, notably, glycosylation for the first time. This was achieved by systematically identifying differentially expressed proteins and PTMs, annotating enriched biological processes and pathways, analyzing protein–protein interactions, and evaluating the kinase activity. The key strength of this study lies in our comprehensive analysis of the molecular mechanisms from multiple perspectives.

The comparison of relative abundance of glycan types between control and radiopharmaceutical-treated groups revealed significant downregulation in the relative abundance of high-mannose glycan structures. The abundance of glycosidases Ganab was significantly decreased in the radiopharmaceutical-treated group. Ganab is the α-subunit of the glucosidase II heterodimer, which removes α1,3-Glc from high-mannose glycans.[40] The reduction in high-mannose glycan-type relative abundance observed following radiopharmaceutical treatment may be associated with the decreased relative abundance of Ganab. The analysis of N-linked glycans revealed that downregulated sialylated glycans predominantly contained NeuGc modifications following ^{225}Ac treatment. Recent studies have shown a correlation between NeuGc levels and risk in cancer, cardiovascular and inflammatory diseases.[41–43] Radiopharmaceutical treatment has been shown to downregulate NeuGc-modified glycans, suggesting that the radiopharmaceutical may exert anti-tumor effects by reducing the NeuGc levels, thereby potentially slowing tumor progression. The analysis of differentially expressed site-specific glycans showed that C1qa–N734–H8N2 exhibited the most significant downregulation. C1qa is the A-chain polypeptide of subcomponent C1qa in the complement system, which is an important component of innate immune response. Recent studies have shown that C1qa can serve as a biomarker for the diagnosis and prognosis of skin cutaneous melanoma and pancreatic cancer.[44–46] Furthermore, our findings indicate that glycosylation predominantly regulates extracellular matrix organization, as shown in Fig. S3C.† This reinforces the significant role of the glycosylated extracellular matrix in cancer progression[47] and provides an additional perspective for the radiopharmaceutical mechanisms.

Additionally, recent phosphoproteome analyses have documented a DNA damage stress response following antigen-targeted radioligand therapy.[18] Consistent with this finding, our phosphoproteomic analysis identified phosphorylation alteration in 57 cell cycle-related proteins (Fig. S2B†) and generated site-specific phosphorylation maps of key cell cycle proteins, including Tp53bp1, Rb1cc1 and Rb1. Based on these results, we hypothesize that ATM and ATR first sense DNA damage and activate the transducer CHEK1. In addition, ATM phosphorylates and activates Tp53bp1,[48] and ATM, Tp53bp1 and CHK1 subsequently phosphorylate p53.[49] Activated p53 inhibits the activity of CDK1 and CDK2, leading to cell cycle arrest in the G1 or G2 phase, respectively (Fig. 4C). Downregulated phosphorylation of Tp53bp1 results in reduced CDK1 and CDK2 kinase activity (Fig. 4D), suggesting that tumor cells may trigger DNA repair mechanisms in response to the radiopharmaceutical treatment. In addition, p53 can enhance the Rb1 pathway by interacting with Rb1cc1.[50] Rb1cc1 activated p16 and dephosphorylated Rb1 by suppressing CDK4.

Proteomic analysis revealed that ^{225}Ac exposure activated the immune system while suppressing cellular metabolism in tumor cells. The relative abundances of numerous mitochondrial proteins were significantly decreased, implying severe disruption of mitochondrial respiratory chain functions by the radiopharmaceutical in tumor cells. Furthermore, recent studies have highlighted a strong correlation between cellular metabolism and immune function within tumor cells, suggesting that targeting metabolic pathways can create a tumor microenvironment more conducive to immune cell infiltration and activation.[35,51,52] Besides, ^{225}Ac activated the hemostasis pathway, and previous studies have reported that radiopharmaceuticals induced severe hematopoietic function failure.[53–55] Given this background, we hypothesize that the upregulation of hemostasis-related proteins in cluster 2 reflects a compensatory activation of the hemostatic pathway in tumor cells following radiopharmaceutical treatment. Our proteomic findings align with these observations, further supporting the interplay between immune responses and metabolic regulation in the context of radiopharmaceutical therapy.

This integrated multi-omics analysis provides a more comprehensive perspective than that a single approach could offer. While the proteome reveals the core functional modules (mitochondrial homeostasis and hematopoietic function), the phosphoproteome and glycoproteome uncover critical regulatory layers (phosphorylation-regulated DNA damage and immune function related to glycosylation) acting upon these modules. The complementary findings highlight the power of simultaneous multi-omics profiling in uncovering the interconnected networks underlying the mechanisms of the radiopharmaceutical. Future research might focus on verifying the detailed role of the impact of phosphorylation of DNA repair proteins, mitochondrial energy metabolism or coagulation function in the mechanism of radiopharmaceutical.

5. Conclusion

This work decrypted the PTM-governed pathway in tumor cells treated with the radiopharmaceutical ^{225}Ac and extended our knowledge of the MoA of radiopharmaceuticals. These results

 This journal is © The Royal Society of Chemistry 2025

Open Access Article. Published on 30 July 2025. Downloaded on 6/14/2026 5:43:12 PM. This article is licensed under a Creative Commons Attribution-NonCommercial 3.0 Unported Licence.

also provide valuable clues for future research on potential radiopharmaceutical resistance and adverse effects. However, these identified potential key proteins and pathways require further biological validation before integration into clinical therapies. Further verification of these proteins in future studies will enable their clinical application as potential therapeutic targets or biomarkers in radiopharmaceutical therapy.

Conflicts of interest

No other potential conflict of interest relevant to this article was reported.

Data availability

Raw MS data generated in this work have been deposited to the ProteomeXchange Consortium *via* the iProX[56,57] partner repository with the data set identifier PXD066148 (in ProteomeXchange) and IPX0012579000 (in iProX). The access link to the data in ProteomeXchange is **https://proteomecentral.proteomexchange.org/cgi/GetDataset?ID=PXD066148**.

Acknowledgements

The authors thank the National Natural Science Foundation of China (22274155 and 22174140), Jiangxi Province Funding (S2024CQKJ1797, 20232ACB203017, 20224BAB206003, and 2024007) and Dalian Institute of Chemical Physics Innovation Funding (DICP I202325) for financial support.

References

1 L. Bodei, K. Herrmann, H. Schöder, A. M. Scott and J. S. Lewis, *Nat. Rev. Clin. Oncol.*, 2022, **19**, 534–550.
2 K. Chakraborty, J. Mondal, J. M. An, J. Park and Y. K. Lee, *Pharmaceutics*, 2023, **15**, 27.
3 J. Sun, Z. Y. Huangfu, J. T. Yang, G. L. Wang, K. Hu, M. Y. Gao and Z. Y. Zhong, *Adv. Drug Delivery Rev.*, 2022, **190**, 24.
4 Y. K. Monfared, P. Heidari, S. J. Klempner, U. Mahmood, A. R. Parikh, T. S. Hong, M. R. Strickland and S. A. Esfahani, *Pharmaceutics*, 2023, **15**, 26.
5 S. Salih, A. Alkatheeri, W. Alomaim and A. Elliyanti, *Molecules*, 2022, **27**, 16.
6 S. Barbieri, G. Baiocco, G. Babini, J. Morini, W. Friedland, M. Buonanno, V. Grilj, D. J. Brenner and A. Ottolenghi, *Radiat. Prot. Dosim.*, 2019, **183**, 121–125.
7 J. P. Ji, Y. P. Zhang, C. E. Redon, W. C. Reinhold, A. P. Chen, L. K. Fogli, S. L. Holbeck, R. E. Parchment, M. Hollingshead, J. E. Tomaszewski, Q. Dudon, Y. Pommier, J. H. Doroshow and W. M. Bonner, *PLoS One*, 2017, **12**, 18.
8 C. E. Redon, A. J. Nakamura, O. Sordet, J. S. Dickey, K. Gouliaeva, B. Tabb, S. Lawrence, R. J. Kinders, W. M. Bonner and O. A. Sedelnikova, *Methods Mol. Biol.*, 2011, **682**, 249–270.
9 A. Stenvall, E. Larsson, B. Holmqvist, S. E. Strand and B. A. Jönsson, *EJNMMI Res.*, 2020, **10**, 12.
10 F. Meissner, J. Geddes-McAlister, M. Mann and M. Bantscheff, *Nat. Rev. Drug Discovery*, 2022, **21**, 637–654.
11 J. W. Lyu, K. Y. Wang and M. L. Ye, *TrAC, Trends Anal. Chem.*, 2020, **124**, 12.
12 L. H. Zhai, K. F. Chen, B. B. Hao and M. J. Tan, *Acta Pharmacol. Sin.*, 2022, **43**, 3112–3129.
13 J. E. Klomp, J. N. Diehl, J. A. Klomp, A. C. Edwards, R. Y. Yang, A. J. Morales, K. E. Taylor, K. Drizyte-Miller, K. L. Bryant, A. Schaefer, J. L. Johnson, E. M. Huntsman, T. M. Yaron, M. Pierobon, E. Baldelli, A. W. Prevatte, N. K. Barker, L. E. Herring, E. F. Petricoin III, L. M. Graves, L. C. Cantley, A. D. Cox, C. J. Der and C. A. Stalnecker, *Science*, 2024, **384**, 21.
14 S. Eckert, N. Berner, K. Kramer, A. Schneider, J. Müller, S. Lechner, S. Brajkovic, A. Sakhteman, C. Graetz, J. Fackler, M. Dudek, M. W. Pfaffl, P. Knolle, S. Wilhelm and B. Kuster, *Nat. Biotechnol.*, 2024, **26**, DOI: **10.1038/s41587-024-02218-y**.
15 L. W. Cao, C. Huang, D. C. Zhou, Y. W. Hu, T. M. Lih, S. R. Savage, K. Krug, D. J. Clark, M. Schnaubelt, L. J. Chen, F. D. Leprevost, R. V. Eguez, W. M. Yang, J. B. Pan, B. Wen, Y. C. Dou, W. Jiang, Y. X. Liao, Z. A. Shi, N. Terekhanova, S. Cao, R. J. H. Lu, Y. Z. Li, R. Y. Liu, H. X. Zhu, P. Ronning, Y. G. Wu, M. A. Wyczalkowski, H. Easwaran, L. Danilova, A. S. Mer, S. Yoo, J. M. Wang, W. K. Liu, B. Haibe-Kains, M. Thiagarajan, S. D. Jewell, G. Hostetter, C. J. Newton, Q. K. Li, M. H. Roehr, D. Fenyö, P. Wang, A. Nesvizhskii, D. R. Mani, G. S. Omenn, E. S. Boja, M. Mesri, A. Robles, H. Rodriguez, O. F. Bathe, D. W. Chan, R. H. Hruban, L. Ding, B. Zhang, H. Zhang and C. Clinical Proteomic Tumor Anal, *Cell*, 2021, **184**, 5031–5052.
16 X. Zhang, T. K. Maity, K. E. Ross, Y. Qi, C. M. Cultraro, M. Bahta, S. Pitts, M. Keswani, S. J. Gao, K. D. P. Nguyen, J. Cowart, F. Kirkali, C. Wu and U. Guha, *Cancer Res.*, 2021, **81**, 3051–3066.
17 X. L. Ding, D. Y. Shang, Y. Cui, X. F. Dong, C. Chen, Y. Y. Zhao, X. L. Li and X. M. Liang, *J. Chromatogr. A*, 2025, **1739**, 11.
18 A. D. Stuparu, J. R. Capri, C. A. L. Meyer, T. M. Le, S. L. Evans-Axelsson, K. Current, M. Lennox, C. E. Mona, W. P. Fendler, J. Calais, M. Eiber, M. Dahlbom, J. Czernin, C. G. Radu, K. Lückerath and R. Slavik, *J. Nucl. Med.*, 2021, **62**, 989–995.
19 M. I. Suominen, K. M. Fagerlund, J. P. Rissanen, Y. M. Konkol, J. P. Morko, Z. Q. Peng, E. J. Alhoniemi, S. K. Laine, E. Corey, D. Mumberg, K. Ziegelbauer, S. M. Käkönen, J. M. Halleen, R. L. Vessella and A. Scholz, *Clin. Cancer Res.*, 2017, **23**, 4335–4346.
20 L. Yu, X. L. Li, Z. M. Guo, X. L. Zhang and X. M. Liang, *Chem. – Eur. J.*, 2009, **15**, 12618–12626.

Open Access Article. Published on 30 July 2025. Downloaded on 6/14/2026 5:43:12 PM. This article is licensed under a Creative Commons Attribution-NonCommercial 3.0 Unported Licence.

21 G. Y. Qing, J. Y. Yan, X. N. He, X. L. Li and X. M. Liang, *TrAC, Trends Anal. Chem.*, 2020, **124**, 13.
22 L. Y. Liu, B. Zhu, Z. Fang, N. Zhang, H. Q. Qin, Z. M. Guo, X. M. Liang, Z. Z. Yao and M. L. Ye, *Anal. Chem.*, 2021, **93**, 7473–7480.
23 L. Y. Liu, L. Liu, Y. Wang, Z. Fang, Y. Y. Bian, W. Y. Zhang, Z. Y. Wang, X. C. Gao, C. R. Zhao, M. M. Tian, X. Y. Liu, H. Q. Qin, Z. M. Guo, X. M. Liang, M. M. Dong, Y. Z. Nie and M. L. Ye, *Adv. Sci.*, 2024, **11**, 14.
24 J. Li, X. F. Dong, Y. Cui, S. Y. Li, C. Chen, X. F. Zhang, X. L. Li, X. M. Liang and Y. Zhu, *J. Chromatogr. A*, 2022, **1681**, 10.
25 J. F. Huang, X. Y. Liu, D. Q. Wang, Y. S. Cui, X. D. Shi, J. Dong, M. L. Ye and L. J. Li, *Anal. Chem.*, 2021, **93**, 8568–8576.
26 Q. Zhang, C. Ma, L. S. Chin, S. Pan and L. Li, *Sci. Adv.*, 2024, **10**, 25.
27 Z. Y. Sun, B. Fu, G. L. Wang, L. Zhang, R. F. Xu, Y. Zhang and H. J. Lu, *Natl. Sci. Rev.*, 2023, **10**, 12.
28 M. Bi, K. Gao, B. Bai and Z. X. Tian, *Anal. Chim. Acta*, 2024, **1322**, 9.
29 X. Hu, J. M. Song, G. G. Ye, M. Zhu, J. F. Lan, L. J. Zeng, Z. Y. Ke and J. Yuan, *J. Med. Virol.*, 2024, **96**, 15.
30 Z. W. Chen, Q. Y. Yu, Q. Yu, J. Johnson, R. Shipman, X. F. Zhong, J. F. Huang, S. Asthana, C. Carlsson, O. Okonkwo and L. J. Li, *Mol. Cell. Proteomics*, 2021, **20**, 16.
31 Y. Q. Zhao, H. B. Li, H. J. Zheng and Q. Jia, *Anal. Chem.*, 2025, **97**, 1135–1142.
32 N. Berois, A. Pittini and E. Osinaga, *Cancers*, 2022, **14**, 42.
33 S. Pan and R. Chen, *Mol. Aspects Med.*, 2022, **86**, 12.
34 W. Guo, Y. L. Cai, X. M. Liu, Y. G. Ji, C. Y. Zhang, L. Y. Wang, W. T. Liao, Y. F. Liu, N. Cui, J. S. Xiang, Z. S. Li, D. Wu and J. X. Li, *Research*, 2023, **6**, 15.
35 Y. Geffen, S. Anand, Y. Akiyama, T. M. Yaron, Y. Z. Song, J. L. Johnson, A. Govindan, O. Babur, Y. Z. Li, E. Huntsman, L. B. Wang, C. Birger, D. I. Heiman, Q. Zhang, M. Miller, Y. E. Maruvka, N. J. Haradhvala, A. Calinawan, S. Belkin, A. Kerelsky, K. R. Clauser, K. Krug, S. Satpathy, S. H. Payne, D. R. Mani, M. A. Gillette, S. M. Dhanasekaran, M. Thiagarajan, M. Mesri, H. Rodriguez, A. I. Robles, S. A. Carr, A. J. Lazar, F. Aguet, L. C. Cantley, L. Ding and G. Getz, *Cell*, 2023, **186**, 50.
36 M. A. Marques, G. C. D. Andrade, J. L. Silva and G. A. P. de Oliveira, *Front. Mol. Biosci.*, 2022, **9**, 25.
37 F. Bonnay, A. Veloso, V. Steinmann, T. Köcher, M. D. Abdusselamoglu, S. Bajaj, E. Rivelles, L. Landskron, H. Esterbauer, R. P. Zinzen and J. A. Knoblich, *Cell*, 2020, **182**, 1490–1507.
38 N. A. Bonekamp, B. Peter, H. S. Hillen, A. Felser, T. Bergbrede, A. Choidas, M. Horn, A. Unger, R. Di Lucrezia, I. Atanassov, X. P. Li, U. Koch, S. Menninger, J. Boros, P. Habenberger, P. Giavalisco, P. Cramer, M. S. Denzel, P. Nussbaumer, B. Klebl, M. Falkenberg, C. M. Gustafsson and N. G. Larsson, *Nature*, 2020, **588**, 712–716.
39 Y. N. Du, Y. N. Li, X. Z. Li, C. R. Jia, L. Wang, Y. Q. Wang, Y. Ding, S. Wang, H. M. Sun, W. Sun, J. S. Tu and C. M. Sun, *Adv. Funct. Mater.*, 2020, **30**, 11.
40 R. De Masi and S. Orlando, *Int. J. Mol. Sci.*, 2022, **23**, 49.
41 S. Bashir, L. K. Fezeu, S. L. Ben-Arye, S. Yehuda, E. M. Reuven, F. S. de Edelenyi, I. Fellah-Hebia, T. Le Tourneau, B. M. Imbert-Marcille, E. B. Drouet, M. Touvier, J. C. Roussel, H. Yu, X. Chen, S. Hercberg, E. Cozzi, J. P. Soulillou, P. Galan and V. Padler-Karavani, *BMC Med.*, 2020, **18**, 19.
42 S. N. Ji, F. Wang, Y. Chen, C. W. Yang, P. W. Zhang, X. B. Zhang, F. A. Troy and B. Wang, *Glycoconjugate J.*, 2017, **34**, 21–30.
43 T. Senage, A. Paul, T. Le Tourneau, I. Fellah-Hebia, M. Vadori, S. Bashir, M. Galinanes, T. Bottio, G. Gerosa, A. Evangelista, L. P. Badano, A. Nassi, C. Costa, G. Cesare, R. A. Manji, C. C. de Monchy, N. Piriou, R. Capoulade, J. M. Serfaty, G. Guimbretiere, E. Dantan, A. Ruiz-Majoral, G. C. du Fou, S. L. Ben-Arye, L. Govani, S. Yehuda, S. B. Abramovitch, R. Amon, E. M. Reuven, Y. Atiya-Nasagi, H. Yu, L. Iop, K. Casos, S. G. Kuguel, A. Blasco-Lucas, E. Permanyer, F. Sbraga, R. Llatjos, G. Moreno-Gonzalez, M. Sanchez-Martinez, M. E. Breimer, J. Holgersson, S. Teneberg, M. Pascual-Gilabert, A. Nonell-Canals, Y. Takeuchi, X. Chen, R. Manez, J. C. Roussel, J. P. Soulillou, E. Cozzi and V. Padler-Karavani, *Nat. Med.*, 2022, **28**, 283–294.
44 S. B. Kemp, N. G. Steele, E. S. Carpenter, K. L. Donahue, G. G. Bushnell, A. H. Morris, S. The, S. M. Orbach, V. R. Sirihorachai, Z. C. Nwosu, C. Espinoza, F. Lima, K. Brown, A. A. Girgis, V. Gunchick, Y. Q. Zhang, C. A. Lyssiotis, T. L. Frankel, F. Bednar, A. Rao, V. Sahai, L. D. Shea, H. C. Crawford and M. P. di Magliano, *Life Sci. Alliance*, 2021, **4**, 17.
45 Z. S. Liang, L. F. Pan, J. K. Shi and L. B. Zhang, *Sci. Rep.*, 2022, **12**, 15.
46 H. L. Yang, D. H. Che, Y. X. Gu and D. S. Cao, *Front. Genet.*, 2022, **13**, 19.
47 A. Rojas, C. Añazco, I. González and P. Araya, *Carcinogenesis*, 2018, **39**, 515–521.
48 B. Lim, Y. Matsui, S. Jung, M. N. Djekidel, W. J. Qi, Z. F. Yuan, X. S. Wang, X. Y. Yang, N. Connolly, A. S. Pilehroud, H. T. Pan, F. Wang, S. M. Pruett-Miller, K. Kavdia, V. Pagala, Y. P. Fan, J. M. Peng, B. S. Xu and J. C. Peng, *PLoS Biol.*, 2024, **22**, 34.
49 A. Shibata and P. A. Jeggo, *DNA Repair*, 2020, **93**, 5.
50 T. Chano, K. Ikebuchi, Y. Ochi, H. Tameno, Y. Tomita, Y. F. Jin, H. Inaji, M. Ishitobi, K. Teramoto, I. Nishimura, K. Minami, H. Inoue, T. Isono, M. Saitoh, T. Shimada, Y. Hisa and H. Okabe, *PLoS One*, 2010, **5**, 10.
51 B. M. Stevens, C. L. Jones, D. A. Pollyea, R. Culp-Hill, A. D'Alessandro, A. Winters, A. Krug, D. Abbott, M. Goosman, S. S. Pei, H. B. Ye, A. E. Gillen, M. W. Becker, M. R. Savona, C. Smith and C. T. Jordan, *Nat. Cancer*, 2020, **1**, 1176–1187.
52 A. Luby and M. C. Alves-Guerra, *Cancers*, 2021, **13**, 28.

 This journal is © The Royal Society of Chemistry 2025

Open Access Article. Published on 30 July 2025. Downloaded on 6/14/2026 5:43:12 PM.
This article is licensed under a Creative Commons Attribution-NonCommercial 3.0 Unported Licence.

53 L. M. Dong, Y. Y. Yang, Y. Lu, C. Lu, J. W. Lv, N. Jiang, Q. X. Xu, Y. Gao, Q. Chang and X. M. Liu, *Phytother. Res.*, 2018, **32**, 741–749.
54 E. Henry and M. L. Arcangeli, *Exp. Hematol.*, 2021, **94**, 11–19.
55 W. X. Li, X. Y. Wang, Y. P. Dong, Q. D. Huo, T. P. Yue, X. Wu, L. Lu, J. L. Zhang, Y. Zhao, H. Dong and D. G. Li, *Aging Cell*, 2023, **22**, 12.
56 J. Ma, T. Chen, S. F. Wu, C. Y. Yang, M. Z. Bai, K. X. Shu, K. L. Li, G. Q. Zhang, Z. Jin, F. C. He, H. Hermjakob and Y. P. Zhu, *Nucleic Acids Res.*, 2019, **47**, D1211–D1217.
57 T. Chen, J. Ma, Y. Liu, Z. G. Chen, N. Xiao, Y. T. Lu, Y. J. Fu, C. Y. Yang, M. S. Li, S. F. Wu, X. Wang, D. S. Li, F. C. He, H. Hermjakob and Y. P. Zhu, *Nucleic Acids Res.*, 2022, **50**, D1522–D1527.